

UC Berkeley

UC Berkeley Previously Published Works

Title

Structural Transformation and Degradation of Cu Oxide Nanocatalysts during Electrochemical CO₂ Reduction

Permalink

<https://escholarship.org/uc/item/4np567cx>

Journal

Journal of the American Chemical Society, 147(8)

ISSN

0002-7863

Authors

Lee, Soo Hong
Acosta, Jaime E Avilés
Lee, Daewon
et al.

Publication Date

2025-02-26

DOI

10.1021/jacs.4c14720

Copyright Information

This work is made available under the terms of a Creative Commons Attribution License, available at <https://creativecommons.org/licenses/by/4.0/>

Peer reviewed

Structural Transformation and Degradation of Cu Oxide Nanocatalysts during Electrochemical CO₂ Reduction

Soo Hong Lee,^{*,|||} Jaime E. Avilés Acosta,^{|||} Daewon Lee, David M. Larson, Hui Li, Junjie Chen, Jinyoung Lee, Ezgi Erdem, Dong Un Lee, Sarah J. Blair, Alessandro Gallo, Haimei Zheng, Adam C. Nielander, Christopher J. Tassone, Thomas F. Jaramillo,^{*} and Walter S. Drisdell^{*}



Cite This: *J. Am. Chem. Soc.* 2025, 147, 6536–6548



Read Online

ACCESS |



Metrics & More



Article Recommendations



Supporting Information

ABSTRACT: The electrochemical CO₂ reduction reaction (CO₂RR) holds enormous potential as a carbon-neutral route to the sustainable production of fuels and platform chemicals. The durability for long-term operation is currently inadequate for commercialization, however, and the underlying deactivation process remains elusive. A fundamental understanding of the degradation mechanism of electrocatalysts, which can dictate the overall device performance, is needed. In this work, we report the structural dynamics and degradation pathway of Cu oxide nanoparticles (CuO_x NPs) during the CO₂RR by using in situ small-angle X-ray scattering (SAXS) and X-ray absorption spectroscopy (XAS). The in situ SAXS reveals a reduction in the size of NPs when subjected to a potential at which no reaction products are detected. At potentials where the CO₂RR starts to occur, CuO_x NPs are agglomerated through a particle migration and coalescence process in the early stage of the reaction, followed by Ostwald ripening (OR) as the dominant degradation mechanism for the remainder of the reaction. As the applied potential becomes more negative, the OR process becomes more dominant, and for the most negative applied potential, OR dominates for the entire reaction time. The morphological changes are linked to a gradual decrease in the formation rate for multicarbon products (C₂H₄ and ethanol). Other reaction parameters, including reaction intermediates and local high pH, induce changes in the agglomeration process and final morphology of the CuO_x NPs electrode, supported by post-mortem ex situ microscopic analysis. The in situ XAS analysis suggests that the CuO_x NPs reduced into the metallic state before the structural transformation was observed. The introduction of high surface area carbon supports with ionomer coating mitigates the degree of structural transformation and detachment of the CuO_x NPs electrode. These findings show the dynamic nature of Cu nanocatalysts during the CO₂RR and can serve as a rational guideline toward a stable catalyst system under electrochemical conditions.



INTRODUCTION

The low-temperature electrochemical conversion of CO₂ into valuable chemicals in aqueous electrolytes has been extensively developed with substantial progress toward industrially relevant performance.^{1–3} Commercially available devices have now demonstrated >3800 h of activity at 190 mA cm⁻² with 95% CO product selectivity,⁴ whereas Cu electrodes have endured more than 200 h maintaining 80% multicarbon (C₂₊) product selectivity.⁵ To be implemented in industry, however, the durability of CO₂ electrolyzers must be improved, ideally demonstrating stable operation for more than 50,000 h, which is the current lifetime of commercial water electrolyzers.⁶ Among the many components in the CO₂ electrolyzer, a detailed understanding of catalyst degradation at the nanoscale is essential to maintain the selectivity and rate of CO₂ reduction during the operation.^{7,8} This degradation is especially severe in Cu-based electrocatalysts, which can convert CO₂ into C₂₊ products, because the Cu surface is

easily reconstructed and corroded during the electrochemical CO₂ reduction reaction (CO₂RR).^{9–11} Therefore, to further understand the failure mode of the Cu-based catalyst, it is imperative to probe how the Cu structure dynamically evolves under CO₂RR conditions.

A key component of the degradation mechanism of electrocatalysts during CO₂RR is the agglomeration of small particles into large structures that can lead to loss of active surface area and activity.^{12,13} One such agglomeration mechanism is particle migration and coalescence (PMC), involving the Brownian motion and subsequent fusion of

Received: October 21, 2024

Revised: January 6, 2025

Accepted: January 8, 2025

Published: January 15, 2025



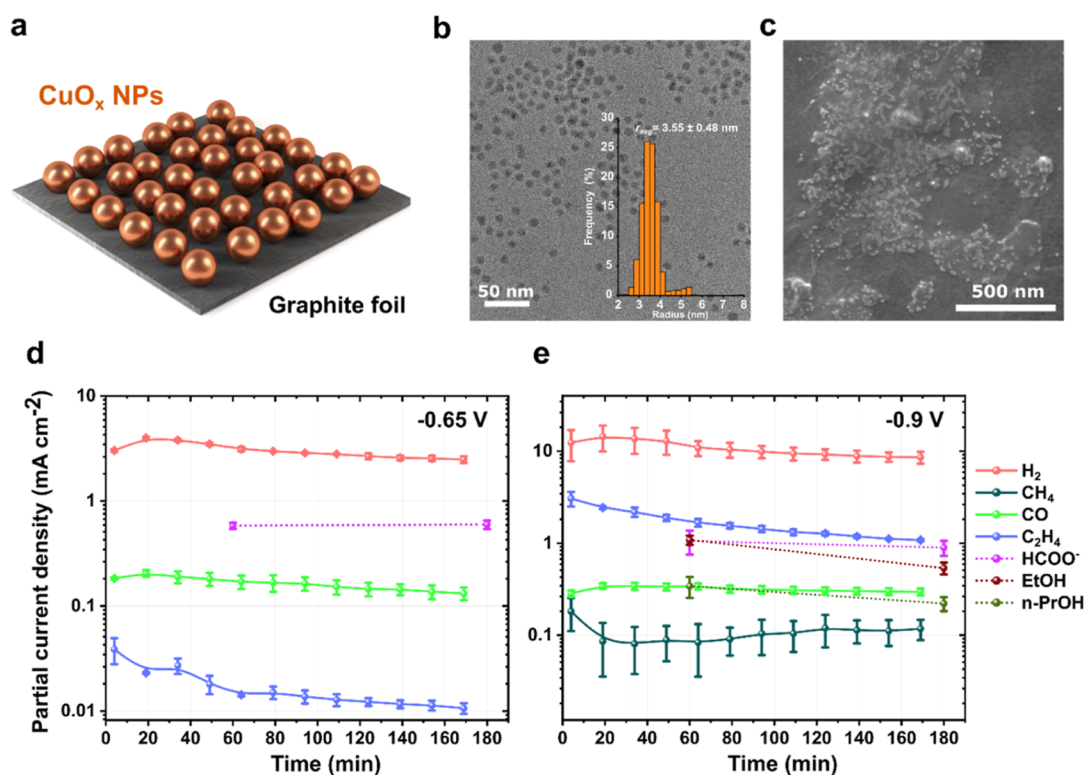


Figure 1. As-synthesized monodisperse CuO_x NPs and their CO₂RR performance. (a) Schematic illustration of CuO_x NPs deposited on the graphite foil using the drop-casting method. (b) Representative TEM image with the corresponding size distribution of as-synthesized CuO_x NPs. (c) SEM image of CuO_x NPs electrode deposited on graphite foil (0.25 mg/cm²). (d,e) Partial current densities for all CO₂RR products obtained from the CuO_x NPs electrode at (d) -0.65 and (e) -0.9 V vs RHE. The y-axis is logarithmic for clarity. The error bars are based on at least two independent measurements.

nanoparticles (NPs) when the NPs approach each other.¹⁴ Under electrical bias, metal electromigration can give rise to the PMC process due to high local current density hotspots.⁷ Another degradation pathway is electrochemical Ostwald ripening (OR), which involves the formation and diffusion of metal species derived from smaller NPs, and their redeposition onto larger particles. In this process, the larger particles are thermodynamically driven to effectively scavenge smaller ones, broadening the particle size distribution with time.¹⁵ The morphological change of Cu-based NPs electrode through the OR process during the CO₂RR has been reported previously,^{16,17} but the dissolution mechanism and chemical identity of Cu species remain elusive.¹⁸ The spontaneous oxidation of Cu to Cu₂O in ambient conditions followed by Cu ion dissolution at open circuit conditions has been reported to induce the OR process at the startup period of the CO₂RR.¹⁹ The continuous generation of highly oxidative hydroxyl radicals in bicarbonate electrolytes accelerates the dissolution of Cu species under CO₂RR conditions.²⁰ The dissolution of Cu catalysts could also be mediated by cathodic corrosion via the dissolution of negatively charged hydride species formed under reducing conditions.²¹ All these mechanisms can contribute to the OR process, leading to the generation of both larger particles and smaller clusters compared to the initial Cu-based catalysts. In addition to these chemical processes, other degradation pathways including catalyst detachment from conductive supports and support deformation are expected to occur simultaneously and intertwine with each other.²² Therefore, the growing importance of stable Cu electrocatalysts demands a fundamental understanding of key

driving forces and kinetics of specific degradation mechanisms during the CO₂RR.

To understand the underlying mechanism of catalyst deactivation during the CO₂RR, several studies have tried to probe morphological changes via post-reaction microscopic analysis.^{14,23} This sole comparison between fresh and spent catalysts only provides static information without insights into the dynamic and transient state of catalysts in response to the reaction conditions. Moreover, removing the spent electrodes from the reaction environments induces rapid oxidation of metallic Cu NPs, which can add artifacts to the final structures.²⁴ In situ transmission electron microscopy (TEM) has recently been utilized to monitor the morphological changes of Cu NPs under CO₂ reduction conditions in real time.^{16,17,25} However, the limited field of view in TEM analysis leads to inconsistent conclusions on which degradation pathway is dominant, and bubble generation under highly negative potentials makes the measurements challenging at the potentials where CO₂ is reduced into C₂₊ products. Thus, it is imperative to track variations in the ensemble-averaged catalyst properties at multiple length scales and high temporal resolution under CO₂RR conditions.

Here, we report the structural transformation and temporal changes in the degradation mechanism of CuO_x NPs under CO₂RR conditions by using in situ small-angle X-ray scattering (SAXS), X-ray absorption near-edge structure (XANES) spectroscopy, and ex situ microscopic analysis. We found that the applied potential during the CO₂RR has a significant impact on the degradation mechanism of CuO_x NPs. At the applied potential of -0.45 V vs the reversible hydrogen

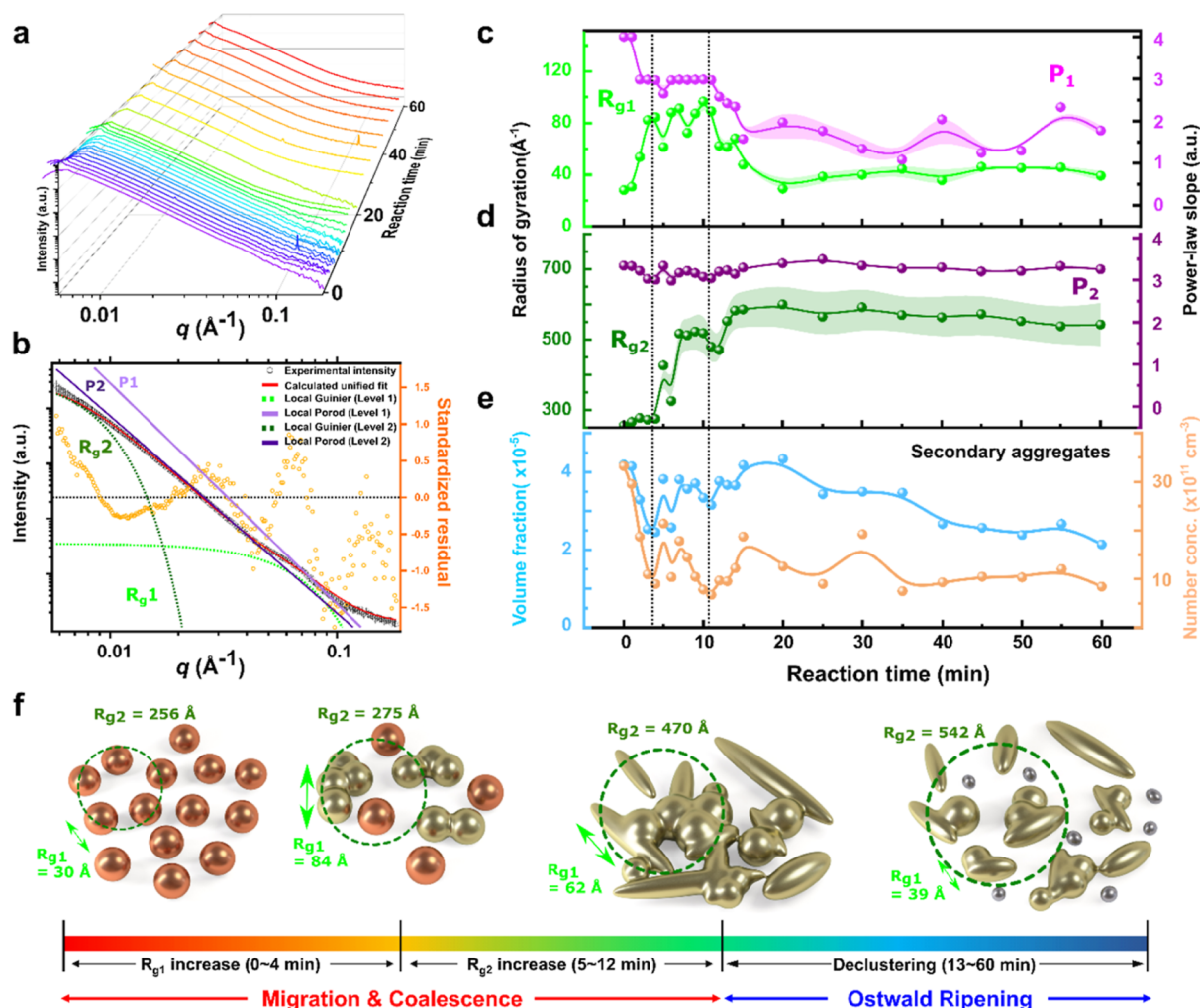


Figure 2. In situ SAXS data from the CuO_x NPs during CO₂RR at -0.65 V. vs RHE. (a) Representative in situ SAXS patterns as a function of reaction time. Both axes are logarithmic. (b) Unified fits involving two structural levels. The one-dimensional SAXS data were obtained from CuO_x NPs electrode under CO₂-purged 0.5 M KHCO₃ at open circuit conditions. The component curves are shown such as the Guinier regime (green dashed line) and power-law scaling regime (light purple line) for the primary NPs, and the Guinier regime (olive dashed line) and power-law scaling regime (purple line) for the secondary aggregates. (c,d) R_g and P values of (c) primary CuO_x NPs and (d) secondary aggregates. (e) Volume fraction (pale blue) and number concentration (pale orange) of the aggregates as a function of reaction time. All parameters are drawn from the unified fit results of SAXS patterns. Error bars result from the fits to the SAXS data. (f) Schematic of the size and morphological evolution of CuO_x NPs during CO₂RR at -0.65 V vs RHE.

electrode (RHE; hereafter, all the potentials are noted vs RHE), we observed a gradual decrease in the size of CuO_x NPs compared to their original size, and did not detect any CO₂RR products. As the applied potential was moved down to -0.65 V, the PMC process governs the agglomeration of CuO_x NPs in the early stage of the CO₂RR, leading to an increase in the size of both primary NPs and secondary aggregates. As the reaction proceeds, the transition of the main degradation mechanism from PMC into OR was observed, resulting in a decrease in the size of primary NPs with broadening size distribution and generation of nanoclusters smaller than the initial CuO_x NPs. The OR process was the dominant degradation mechanism over the whole reaction time at the most negative potential of -0.9 V. Through a comparative analysis of SAXS data obtained under CO₂ and Ar-purged electrolytes, we conclude that the PMC process is primarily driven by electromigration and further enhanced by reaction intermediates. In contrast, the OR process is mediated by local high pH near the electrode, resulting in a reduction in the size

of primary NPs. The agglomeration and detachment of CuO_x NPs were mitigated by using carbon supports with a high surface area and ionomer coatings. These results on how electrochemical parameters affect the structural stability of nanocatalysts provide strategies that can mitigate degradation under a reducing reaction microenvironment.

RESULTS AND DISCUSSION

CuO_x NPs as a Model Catalyst for In Situ SAXS Study.

We first synthesized and characterized monodisperse CuO_x NPs as a model electrocatalyst with an average radius (r_{avg}) of 3.55 ± 0.48 nm, confirmed by transmission electron microscopy (TEM, Figure 1a,b). TEM and grazing incidence X-ray diffraction (GIXRD) analysis demonstrated that the deposited CuO_x NP is a mixture of metallic Cu, Cu₂O, and CuO (Figure S1a-c). The as-synthesized CuO_x NPs were directly deposited onto graphite foil with a loading amount of ~0.25 mg/cm², generating a catalyst layer with a thickness of 1–2 μm (Figures 1c and S1d). We selected this loading

amount based on distinct features observed in the SAXS patterns obtained under open circuit conditions (Figure S2). The observed features were associated with the Guinier region derived from the 6–7 nm CuO_x NP ensemble, and were evident at loading levels above ~0.2 mg/cm². We monitored the partial current densities for all CO₂RR products obtained from the CuO_x NPs electrode at –0.65 and –0.9 V (Figure 1d,e). Over the course of 3 h of reaction, the partial current densities of C₂ products decreased rapidly, including ethylene at both overpotentials and ethanol at –0.9 V. No CO₂RR products were detected at –0.45 V due to their generation below the detection limit as a result of the low current densities (Figure S3). It should be noted that the total Faradaic efficiency (FE) below 100% can potentially be attributed to the crossover of liquid products toward the anode.^{26,27} The resulting CuO_x NPs electrode was incorporated into a custom-built electrochemical flow cell that is designed to enable in situ SAXS measurements under CO₂RR conditions (Figures S4a,b). The thickness of the electrolyte pathway (6 mm) is minimized to mitigate attenuation of the X-ray transmission by the electrolyte. The minimized electrolyte pathway can cause bubbles to block the catalyst layer during the gas-evolving CO₂RR and hydrogen evolution reaction (HER). This blockage leads to discontinuous current density profiles due to limited reactant availability (Figure S4c). To facilitate the detachment of gas bubbles from the electrode surface, we added anionic hydrotropes (5 mM sodium *p*-toluenesulfonate) into the electrolyte that can decrease the bubble size and residence time by reducing the surface tension.²⁸ After adding the hydrotropes, stable current densities were recorded under CO₂- and Ar-purged electrolyte up to –0.9 V (Figure S4d,e). The hydrotropes do not alter the CO₂RR performance (Figure S5) or the size evolution behavior of CuO_x NPs during the reaction (discussed below). This cell configuration exhibited no apparent X-ray beam damage, as evidenced by the consistent size stability observed in CuO_x NPs during continuous SAXS measurements at open circuit conditions (Figure S6).

In Situ SAXS Study during CO₂RR. To monitor the structural transformation of CuO_x NPs, we collected in situ SAXS spectra for 1 h of electrolysis with an interval of 1 min at –0.65 V under CO₂RR conditions (Figure 2a). The global unified function was employed to fit the SAXS pattern,²⁹ assuming that the Cu structure, derived from the initial CuO_x NPs, consisted of two distinct structural levels: primary CuO_x NPs and secondary aggregates (Figure 2b). This fitting method has been employed for characterizing the changes in electrocatalysts and thermal catalysts, particularly when the primary NPs aggregate into secondary structures.^{30–32} The fitting result allows us to estimate the radius of gyration (R_g) and the power-law slope (P) of primary NPs (R_{g1} and P_1 , Figure 2c) and of secondary aggregates (R_{g2} and P_2 , Figure 2d), respectively, with high reliability ($0.9 \leq \chi^2 \leq 1.1$, Figure S7). The R_g value is related to the size depending on the structural model, and the P value reflects the morphology of the underlying structure.³³ The calculated radius of the initial CuO_x NPs at open circuit conditions was 3.62 ± 0.38 nm in the sphere model, which agrees with the size derived from the TEM. The fitting result also yields the number density and volume fraction of the secondary aggregates by calculating the Porod invariant Q (Figure 2e). The detailed theory and application of the unified fit are discussed in the Supporting Information. The P_1 values before 3 min were close to 4,

corresponding to spherical particles, whereas they showed a deviation from the value of 4 after 3 min, implying changes in the structure, such as particle elongation or surface roughening (Figure 2c). The P_2 values remained between 3 and 4 during the whole reaction time, which represents surface fractal morphology (Figure 2d). The size distributions can be calculated under the assumption of spherical particles ($P_1 = 4$) and log-normal distributions.^{29,34}

Quantitative SAXS analysis revealed that the growth of CuO_x NPs at –0.65 V occurred in three distinct periods (Figure 2f). Until 4 min of reaction, the R_{g1} value showed an increase and reached up to ~84 Å (Figure 2c). The aggregates also started to grow in this period, but the increase in the R_{g2} value did not exceed 10% (Figure 2d). The volume fraction and number concentration of aggregates rapidly decreased in this period, possibly indicating the particle detachment from the electrode as well as migration out of the irradiated volume (Figure 2e). This result suggests that initial aggregation of neighboring CuO_x NPs during the early stages of the reaction occurred through the PMC mechanism. Previous research has shown that the electromigration of the metal can serve as a driving force for the aggregation of nanostructures in response to an applied electric field and the flow of current.^{7,35} In the next period (5–12 min), the R_{g2} value rapidly increased up to ~522 Å within 3 min and sustained this level. Meanwhile, the R_{g1} value exhibited oscillations between 65 and 90 Å, with an overall increasing trend. The rapid growth of aggregates without any prominent size decrease in primary CuO_x NPs indicates that an increase in R_{g2} occurs through the sintering of pre-existing aggregates. The rapid growth of primary CuO_x NPs in the initial stage, followed by significant increase in secondary aggregates suggests the dominance of PMC in the size change mechanism. The agglomeration process decelerated as the reaction continued.

During the last period (13–60 min), declustering behavior was observed in the primary CuO_x NPs, while aggregate size remained at or above the upper SAXS detection limit of ~150 nm. The R_{g1} values decreased rapidly until 20 min with a broadening size distribution (Figure S8), indicating the dissolution of transient Cu species and redeposition onto the large particles, according to the OR process.^{18,36} We observed the formation of micrometer-sized CuO_x agglomerates via post-mortem ex situ scanning electron microscopy (SEM) with energy-dispersive X-ray spectroscopy (EDS) analysis (Figure S9a–d). These large particles can keep growing by consuming the CuO_x NPs even after the PMC mechanism for agglomeration is no longer dominant. We also found evidence of the emergence of Cu clusters with a radius of about 2 nm (Figure S9e,f), further indicating that the OR process was dominant. Thus, the results indicate that a mechanistic transition from PMC to OR process took place as the CO₂RR proceeded at –0.65 V, resulting in a hierarchical Cu structure ranging from micrometer-sized agglomerates to nanoscale clusters (Figure 2f). This finding demonstrates that employing in situ SAXS in conjunction with the unified fitting method affords a comprehensive insight into the degradation mechanism of catalysts, as it enables the monitoring of the size and morphology evolution of CuO_x NPs during the CO₂RR.

Structural Transformation of CuO_x NPs Depending on the Applied Potentials. To investigate the structural evolution of CuO_x NPs depending on the applied potentials during the CO₂RR, we collected in situ SAXS data (Figure

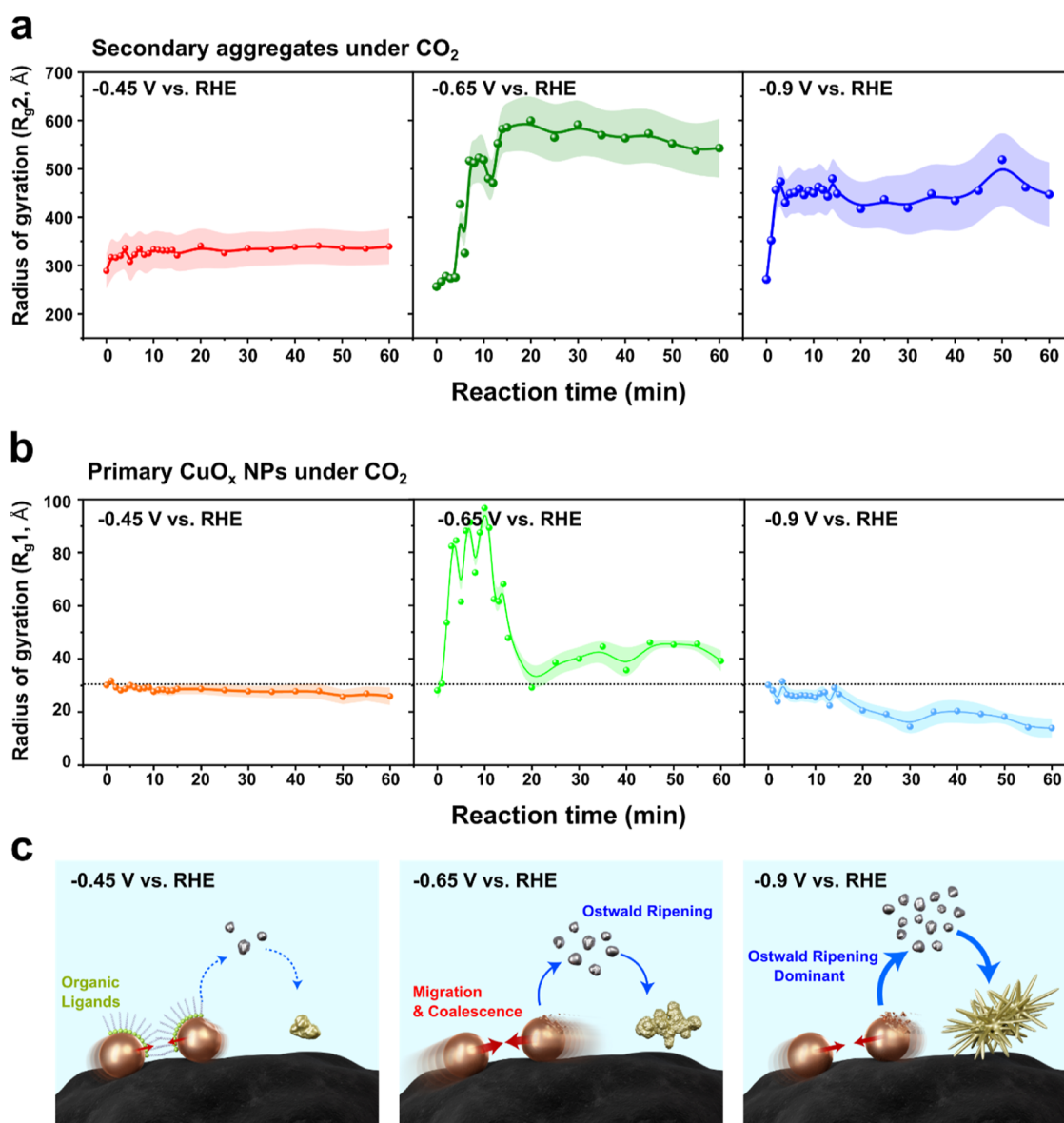


Figure 3. Size evolution of CuO_x NPs and secondary aggregates during CO₂RR at different overpotentials. (a,b) Temporal changes in the R_g values of (a) secondary aggregates (R_{g2}) and (b) primary CuO_x NPs (R_{g1}) during the CO₂RR as a function of reaction time and the applied potentials. The error bars indicate the estimated standard error from the least-squares fit. The dotted line in b indicates the initial radius of CuO_x NPs at the open circuit state. (c) Schematic illustration of the structural transformation of CuO_x NPs during CO₂RR depending on the applied potentials.

S10) and conducted post-mortem microscopy on the samples after reaction under CO₂-purged electrolyte (Figures S11 and S12). By using the unified fit, we tracked and compared the size evolution of secondary aggregates (Figure 3a) and primary CuO_x NPs (Figure 3b) with the applied potentials from -0.45 to -0.9 V. At -0.45 V, the growth of aggregates was not evident and the initial size of primary CuO_x NPs remained constant until 15 min. The R_{g1} value slightly decreased from 30 to 25 Å with a broadening size distribution after 15 min, indicating that the OR process took place (Figure S13a). The SAXS analysis was correlated to the ex situ SEM, EDS, and TEM data analysis. We observed micrometer-sized particles on top of the catalyst layer, which turned out to be organic residues derived from ligands used in the preparation of the CuO_x NPs (Figure S11a–c). The organic residues were the only micrometer-sized structures observed for the sample run at -0.45 V, with no evidence of micrometer-sized Cu

agglomerates (Figure S11d). The phosphonic acid-based ligands utilized in this study have previously been demonstrated to desorb from the surface of CuO_x NPs at negative potentials corresponding to the CO₂RR.³⁷ We confirmed the initiation of ligand desorption at approximately 0 V, and a residual amount of ligands, measuring below 1 wt %, seems to persist on the electrode after applying more negative potentials than -0.45 V (Figure S14). This result suggests that the PMC mechanism could be suppressed at -0.45 V due to the protective role of surface ligands against agglomeration among the CuO_x NPs. However, this protection may not be effective during the CO₂RR since the reaction rate is slow at -0.45 V (Figure S3). Considering the marginal size reduction observed after a 15 min application of -0.45 V, we infer that the structural transformation of CuO_x NPs initiates before the onset of the CO₂RR.

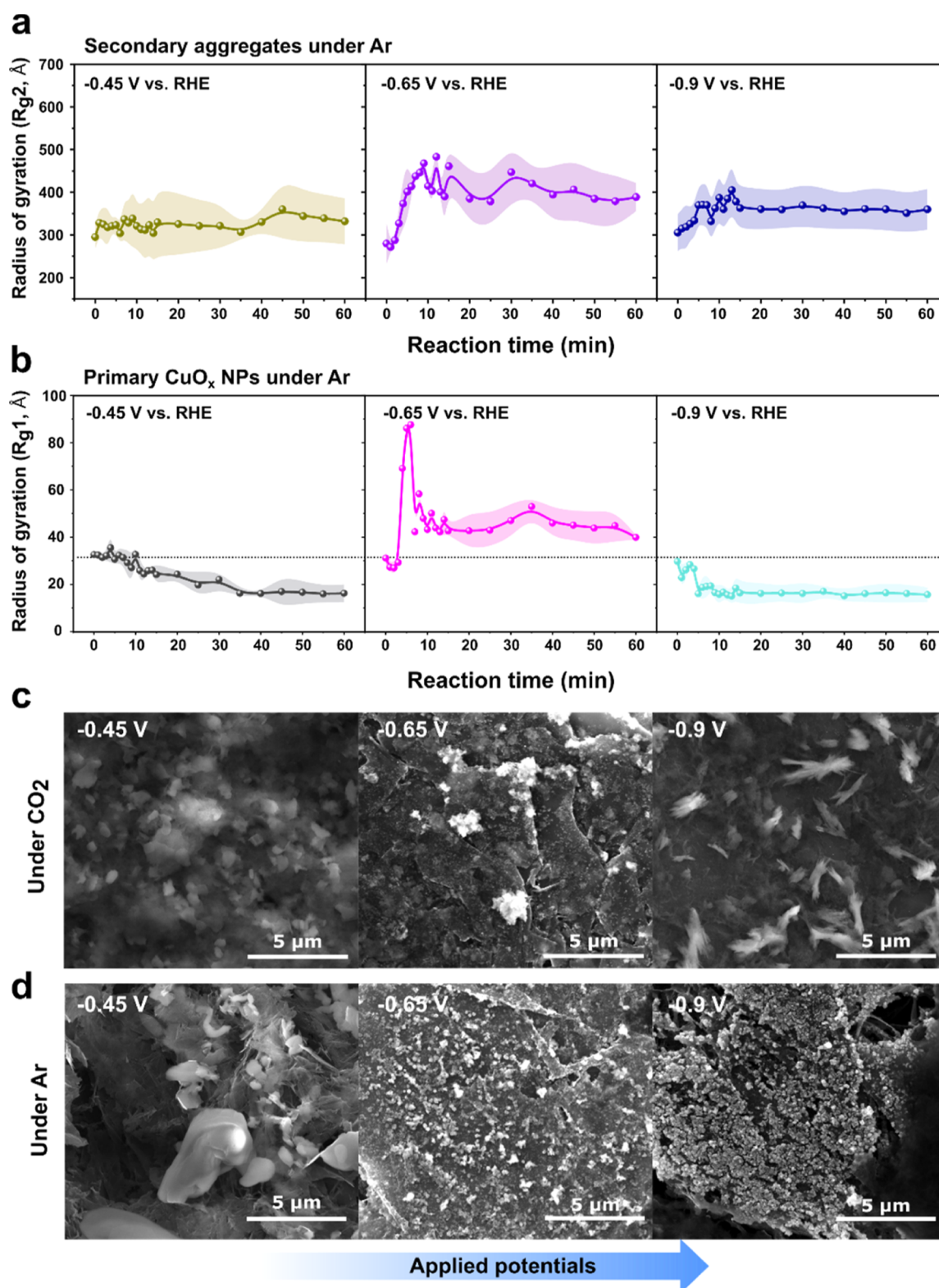


Figure 4. Differences in the structural dynamics under the CO_2RR and HER conditions. (a,b) Temporal changes in the R_g of (a) secondary aggregates (R_{g2}) and (b) primary CuO_x NPs (R_{g1}) under Ar-purged 0.5 M $\text{K}_x\text{H}_{3-x}\text{PO}_4$ electrolyte at different applied potentials. The error bars represent the estimated error from the least-squares fit. The dotted line in b indicates the initial radius of CuO_x NPs at the open circuit state. (c,d) Post-mortem, ex situ SEM images of CuO_x NPs electrode under the (c) CO_2^- and (d) Ar-purged electrolytes as a function of the applied potentials.

By contrast, the structural changes of CuO_x NPs at -0.9 V showed an immediate decrease in R_{g1} value from 32 to 25 Å within 10 min and a size broadening of primary CuO_x NPs as the reaction started, and this trend continued throughout the 1

h of electrolysis (Figures 3b and S13b). An increase in R_{g2} value from 271 to ~ 450 Å was observed within 3 min, followed by a relatively stable value of ~ 450 Å for the remainder of the reaction. The growth of aggregates without an increase in R_{g1}

value, and the broadening size distribution of primary CuO_x NPs, imply that the OR process was the prevailing mechanism throughout the agglomeration process. The post-mortem microscopic analysis revealed that dendritic CuO_x particles with a size up to $\sim 5 \mu\text{m}$ were formed. In addition, we identified Cu clusters adjacent to the aggregates with a radius as small as $\sim 1.3 \text{ nm}$, which is notably smaller than the original NPs with a radius of 3.5 nm (Figure S12) and also indicative of OR. The PMC mechanism in the early period of the reaction cannot be completely excluded, due to the existence of polycrystalline aggregates comprised of fused and elongated rod-shaped NPs in the TEM images. The trend of structural changes was reproduced in another CuO_x NPs sample (Figure S15). Thus, these results strongly suggest the OR mechanism dominated the structural evolution of CuO_x NPs at -0.9 V under CO_2 -purged electrolyte. Figure 3c illustrates the morphological evolution of CuO_x NPs during the CO_2RR depending on the applied potential. As the negative potentials varied from -0.45 to -0.65 V , the degree of structural reconstruction became increasingly prominent. This reconstruction was characterized by the PMC observed during the initial stages of the reaction, followed by the OR process. The emergence of PMC-driven agglomeration in the early period could be due to the accelerated electromigration rate of Cu at the more negative potential, along with the desorption of the ligands at -0.65 V . As CO_2RR progresses, the growth of primary NPs and secondary structures slows the rate of PMC-driven agglomeration. Consequently, the rate of OR surpasses that of PMC, leading to the declustering of primary NPs. This dynamic interaction accounts for the abrupt change in R_{g1} values observed specifically at -0.65 V . The declustering of NPs appears to be accelerated with more negative potential as well, which could be due to OR dominating over other agglomeration processes at -0.9 V . The generation of Cu clusters coincides with the decrease in FE for C_2 products, consistent with previous findings that C–C coupling is less favorable in small-sized NPs and clusters.^{38,39} The results demonstrated that both PMC and OR mechanisms can operate simultaneously and shift dynamically during the reaction, depending on the applied potential and reaction time.

Investigation of Reaction Parameters Governing Structural Transformation. To study the driving force behind the structural evolution of CuO_x NPs in response to reaction conditions, we measured the reconstruction of CuO_x NPs with different applied potentials under Ar-purged $0.5 \text{ M K}_x\text{H}_{3-x}\text{PO}_4$ electrolyte by using in situ SAXS (Figure 4a,b) and post-mortem microscopic analysis (Figures S16–S18). A similar trend of size changes in the primary CuO_x NPs and secondary aggregates from -0.45 to -0.9 V was observed compared to that of the samples under CO_2 -purged electrolyte. At a potential of -0.45 V , the growth of secondary aggregates was not evident and a reduction in the size of primary CuO_x NPs was observed after 10 min, which was attributed to the OR process occurring during the later stages of the reaction. A potential of -0.65 V resulted in a rapid increase in both R_{g1} and R_{g2} values, which can be ascribed to the PMC operating during the early stages of the reaction. After 6 min, a rapid decline in R_{g1} values from ~ 80 to $\sim 47 \text{ \AA}$ was observed, indicating that the OR process had taken over. At -0.9 V , an immediate decrease in R_{g1} values with a broadening of the size distribution was discovered, suggesting the prevalence of the OR process throughout the entire reaction. The P_2 values under both CO_2 and Ar-purged electrolytes remained within

the values of 3 and 4 regardless of the reaction conditions, indicating the surface fractal structure of secondary aggregates (Figure S19). Similar behavior in the reconstruction under CO_2 - and Ar-purged electrolytes indicates that the applied potential is one of the main factors to drive size and morphological changes during the CO_2RR .

Another factor to consider is the high local pH near the electrode surface, caused by the production of OH^- ions during the CO_2RR and HER. To investigate the effect of local pH on the reconstruction of CuO_x NPs, we conducted measurements and analysis of in situ SAXS data of CuO_x NPs under Ar-purged 0.5 M KOH electrolytes ($\text{pH} > 13$, Figure S20). The fitting results demonstrated a sudden decrease in R_{g1} values, reaching $\sim 20 \text{ \AA}$ within 5 min at -0.45 V , and $\sim 16 \text{ \AA}$ within 2–3 min at -0.65 and -0.9 V , respectively. This rapid reduction in the size of the primary CuO_x NPs can be attributed to the instability of CuO_x NPs in $\text{pH} > 13$ and the positive open circuit voltage value ($\sim 0.8 \text{ V}$), causing oxidation and dissolution of the CuO_x NPs (Note S1).^{16,19} The presence of dissolved Cu ions and/or species, which are generated during the open-circuit period, along with the reduction of the Cu oxide/hydroxide layer, can contribute to a high rate of small cluster formation when a cathodic bias is applied. This process ultimately can lead to a sudden reduction in the size of the primary CuO_x NPs, attributed to the development of a high local pH near the electrode, as both the CO_2RR and the HER continue.

The main difference in the structural evolution of CuO_x NPs under CO_2 - and Ar-purged electrolytes is a faster decline of R_{g1} values from -0.45 to -0.9 V under Ar-purge than the samples under CO_2 -purged electrolyte (Figure S21a). The R_{g2} values calculated at -0.65 V were found to be below 450 \AA , which are smaller than those calculated for the CO_2 -purged electrolyte (Figure S21b). At a potential of -0.45 V , a decrease in R_{g1} was accelerated from ~ 30 to $\sim 16 \text{ \AA}$ after 10 min (Figure S21c). The declustering of primary CuO_x NPs was observed within 6 min at -0.65 V , which was faster than the samples under CO_2 -purged electrolyte. Under the potential of -0.9 V , the R_{g1} values exhibited a more rapid decrease from ~ 30 to $\sim 18 \text{ \AA}$ within 5 min, accompanied by a broadening size distribution (Figure S21d). The morphological difference in the samples under CO_2 - and Ar-purged electrolytes was also revealed in the formation of micrometer-sized particles depending on the applied potentials. The ex situ SEM analysis demonstrated that micrometer-sized dendritic particles formed under CO_2RR conditions (Figure 4c), whereas the formation of micrometer-sized particles was partially suppressed under Ar conditions (Figure 4d). The delayed declustering behavior of CuO_x NPs electrode²³ and the development of dendritic structures under CO_2 conditions¹⁷ have been observed previously. These unique features can provide new insights into other factors that drive degradation during the CO_2RR .

We also examined the impact of the oxidation states of CuO_x NPs during the CO_2RR and HER on morphological changes. We collected in situ XANES spectra as a function of applied potentials in CO_2 - and Ar-purged electrolytes, and the first derivatives of the XANES spectra were used to evaluate the oxidation states of CuO_x NPs (Figures S22 and S23). Within the potential range of -0.45 to -0.7 V , the CuO_x NPs remained in a metallic state (Figure S24). The CuO_x NPs were fully reduced into metallic states below -0.45 V under CO_2 -purged electrolytes within 2 min of the reaction. Considering that the size of CuO_x NPs did not significantly change in 2 min

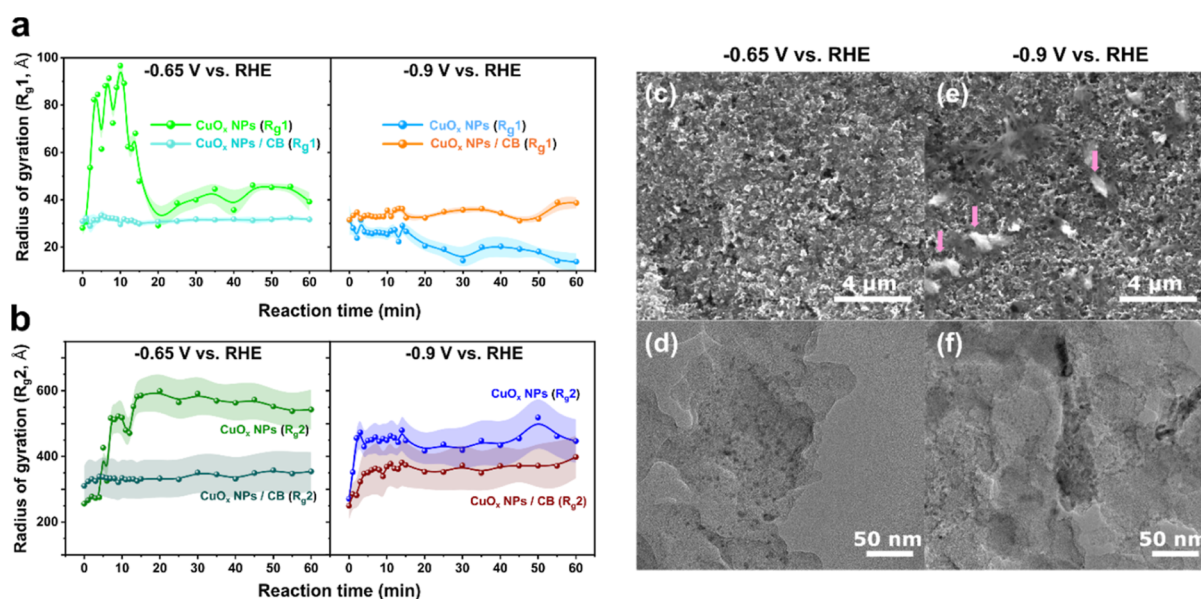


Figure 5. Carbon supports with a high surface area mitigate severe aggregation of CuO_x NPs during the CO₂RR. (a,b) Temporal changes in the R_g values of (a) primary CuO_x NPs and (b) secondary aggregates for the CuO_x NPs/CB electrode as a function of the reaction time at -0.65 and -0.9 V under CO₂-purged 0.5 M KHCO₃ electrolyte. Error bars result from the least-squares fits of the SAXS data. (c–f) Post-mortem and ex situ SEM and TEM images of CuO_x NPs/CB electrodes under the CO₂-purged 0.5 M KHCO₃ electrolyte at (c,d) -0.65 and (e,f) -0.9 V, respectively.

as confirmed by SAXS analysis, this result suggests that the oxidation states do not play a major role in the ensemble-averaged structural evolution of CuO_x NPs during the CO₂RR. We also examined the influence of hydrotropes on morphological changes in the CuO_x electrode through in situ SAXS measurements (Figure S25). We tested the electrode with half the loading amount of NPs (0.125 mg/cm²) compared to the electrode with hydrotropes, as gas bubbles impede reliable measurements. Despite the varying NP loading amounts, the fitting results obtained at -0.9 V showed a similar trend compared to the electrode with hydrotropes, indicating no discernible impact of hydrotropes on morphological changes. However, the $R_{g,2}$ value remained below 400 Å and required over 20 min to reach its maximum. This growth rate of secondary aggregates is slower than that observed for electrodes with a loading level of 0.25 mg/cm² (Figure 3a). Based on these results, we conclude that while the overall trends of structural transformations—including PMC-driven agglomeration and OR processes—remain consistent, the transformation rate is influenced by the loading level.

Next, we consider the role of surface-bound reaction intermediates, such as *CO for the CO₂RR and *H for the HER, to elucidate the distinct structural changes observed under CO₂ and Ar conditions. The CO* intermediate is recognized for inducing transient Cu dissolution during the CO₂RR by forming a Cu–CO complex.¹⁸ In the early stages of the CO₂RR, the predominant agglomeration was mediated by the PMC process induced by the electromigration of CuO_x NPs. Furthermore, this process could be intensified by the CO* intermediate-induced Cu dissolution and redeposition. The enhanced agglomeration by CO* intermediates can account for the delayed declustering behavior and larger size of aggregates observed under CO₂ condition compared to those of Ar condition. The formation of dendrite structure under CO₂ condition can be explained by the wet electromigration condition that enhances the migration of metal species in the presence of electrolytes.³⁵ Under electric bias,

the dissolved metal species tend to deposit at localized needles or spikes, because the higher current density at their tips considerably enhances the probability of additional deposition.⁴⁰ Due to the resulting concentration gradients, the formation of a dendritic structure can occur, which is consistent with our findings under CO₂-purged electrolyte. Through a comparison of the in situ SAXS data acquired under CO₂RR and HER conditions, we deduce that the agglomeration process is primarily driven by electromigration induced by the applied potential, mainly through the PMC mechanism. Additionally, this process can be further enhanced by CO₂RR intermediates. As the CO₂RR progresses, the degradation process is then replaced by the OR process induced by high alkalinity near the electrode and the Cu dissolution, leading to a rapid reduction in the size of primary CuO_x. The observed structural transformation, including PMC-driven agglomeration induced by electromigration and CO intermediates, as well as the OR mechanism driven by Cu dissolution, may also occur in other Cu-based catalysts. The rate and extent of these transformations, however, depend on the size, shape, and morphologies of Cu electrocatalysts, as reported in previous studies.^{7,25}

Mitigation of Degradation of CuO_x NPs by Carbon Supports. As agglomeration of CuO_x NPs through the PMC process in the early period and the OR process in the later period is the main degradation mechanism during the CO₂RR, various approaches can be used to mitigate degradation. The common practice of using carbon black as a support and Nafion ionomer as a binder is employed not only to enhance electrical and ionic conductivity but also to shield the electrocatalysts from various degradation pathways.²² Our results suggest that this protective scheme could be effective, as it increases the interparticle distance between CuO_x NPs, thereby alleviating the PMC process, and improving the metal–support interaction to mitigate dissolution for OR process. The individual CuO_x NPs were isolated on the support surface as confirmed by TEM, and high current

densities were observed under both CO₂ and Ar-purged electrolytes (CuO_x NPs/CB, Figure S26). We tested this hypothesis by investigating the role of protection scheme in the structural reconstruction of CuO_x NPs with in situ SAXS measurements (Figure S27). The changes in the R_{g1} value at -0.65 V under CO₂-purged electrolyte indicated that the agglomeration process through the PMC mechanism in the early period of the reaction (<5 min) was suppressed in the case of CuO_x NPs/CB (Figure 5a). The R_{g2} values of CuO_x NPs/CB remained stable at ~ 340 Å throughout the reaction time, which is lower than those of unsupported CuO_x NPs (up to ~ 550 Å, Figure 5b). The post-mortem ex situ SEM and TEM analysis revealed that the formation of micro-sized Cu agglomerates was prevented, but Cu clusters with a radius as small as ~ 1.3 nm were still observed (Figure 5c,d). These results illustrate that the OR process was only partially suppressed, even though the carbon supports helped to relieve the agglomeration of CuO_x NPs through the PMC process.

For CuO_x NPs/CB at -0.9 V in CO₂-purged electrolytes, the R_{g1} values remained stable, maintaining their initial value of ~ 32 Å throughout the 1 h electrolysis period (Figure 5a). While the average R_{g2} values were lower than those of unsupported CuO_x NPs electrodes, no significant differences in the R_{g2} values were observed within the error ranges (~ 362 Å, Figure 5b). This trend in structural changes in the CuO_x NPs/CB was similar for the samples under the Ar-purged electrolytes, indicating that the carbon supports and ionomer coatings alleviate the PMC and OR process of CuO_x NPs regardless of reaction conditions (Figure S28). The suppression of structural changes in the CuO_x NPs/CB is also linked to the stability in partial current densities and FE for ethylene during the 3 h of reaction (Figure S29). However, post-mortem ex situ SEM and TEM analysis revealed the generation of micro-sized particles and small clusters locally, attributed to the OR process (Figure 5e,f). These findings suggest that completely preventing the OR process at very negative potentials requires additional protection to reduce the corrosion and consequent dissolution of CuO_x NPs into electrolytes.

The detachment of CuO_x NPs was also mitigated by utilizing the carbon supports and ionomer. The post-mortem EDS mapping analysis of the unsupported CuO_x NPs demonstrated that the CuO_x NPs detached from the graphite foil when a negative bias was applied (Figure S30). The CuO_x NPs/CB electrode exhibited higher values of volume fraction and number density compared to those of unsupported CuO_x NPs, indicating a reduction in NP detachment (Figure S31).

Based on these findings, various strategies can be devised to mitigate Cu nanocatalyst degradation during CO₂RR. For the agglomeration process driven by electromigration, alloying Cu with Al could decrease the rates of Cu electromigration transport, as previously reported in the development of reliable integrated circuits.⁴¹ In polycrystalline Cu structures, electromigration predominantly occurs through grain boundaries, where active sites for CO₂RR are known to be located.^{25,42} The presence of Al can retard the transport rate of Cu in grain boundaries due to the formation of Al-vacancy complexes at the grain boundaries.⁴³ As Cu–Al alloy has also been recognized as an efficient CO₂RR catalyst with high selectivity toward ethylene,⁴⁴ alloying Cu with other metals could be an excellent approach for developing both efficient and durable electrocatalysts for the CO₂RR. To mitigate the declustering process induced by local high pH, it is crucial to manage a

balance between CO₂ mass transport and reaction rates to control pH values near the electrode. While local alkaline pH has been attributed to parasitic HER suppression and enhanced selectivity toward hydrocarbon products, it must be balanced with the instability of Cu under local alkaline pH conditions in the development of durable CO₂RR catalysts. Mitigation strategies may involve physical coatings with carbon materials to shield the Cu surface,⁴⁵ or alloying with Ga metal to enhance resistance against Cu dissolution.⁴⁶ These strategies should also be validated under high current density conditions in membrane electrode assembly (MEA) and flow cell systems, which possess a different three-phase interface (gas–liquid–catalyst) compared to our study. Additionally, real-time CO₂RR product measurement is crucial due to the significant structural transformations occurring during the initial reaction stages; however, the currently available detection methods have limitations. Future studies will focus on addressing these challenges, enabling rapid quantitative analysis during the early stages of the reaction and extending the applicability of our findings to MEA and flow cell systems.

CONCLUSIONS

In summary, we investigated the structural dynamics and degradation mechanism of monodisperse CuO_x NPs under CO₂RR conditions. By using in situ SAXS and post-mortem ex situ microscopic analysis, the mechanism of structural transformation of CuO_x NPs was demonstrated to be highly dependent on the applied potential during the CO₂RR. At an applied potential of -0.45 V, where no detectable CO₂RR occurred, the growth of secondary aggregates was suppressed due to the protective role of organic ligands on the surface, and the OR process occurred in the later stage of the reaction. For more negative applied potentials down to -0.65 V, the ensembles of CuO_x NPs agglomerated through the PMC process in the early stage of the reaction, and subsequently, the dominant degradation mechanism changed into the OR process. At the most negative potential of -0.9 V, the OR process was dominant throughout the whole reaction time. A comparative analysis of SAXS data under CO₂RR and HER conditions revealed that electromigration, primarily via the PMC mechanism, drives agglomeration, which can be enhanced by CO₂RR intermediates. As the CO₂RR progresses, OR processes dominate due to the high local pH near the electrode, resulting in a rapid reduction in the size of primary CuO_x NPs. In situ quick-scanning XANES suggests that the CuO_x NPs were fully reduced into metallic Cu before the onset of structural changes. While the introduction of carbon support and ionomer coatings mitigated the detachment and agglomeration of CuO_x NPs, structural transformation still took place through the OR process. Our study provides fundamental insights into the structural dynamics of nanocatalysts and establishes a basis for the rational design of highly stable electrocatalysts under CO₂RR conditions. The previously developed strategies against the degradation, including the introduction of support materials, physical barriers on the surface, and alloying with second metals, could be utilized. Additionally, new strategies inhibiting PMC and OR processes and preventing catalyst detachment should be developed to meet the durability requirements for commercialization.

EXPERIMENTAL SECTION

Synthesis of CuO_x NPs. Ten mL of trioctylamine (Sigma-Aldrich, 98%) in a three-neck flask was degassed with N₂ gas at 130 °C for 30

min to remove any moisture in the solvent and cooled to room temperature. One mmol of copper (I) acetate (Sigma-Aldrich, 97%) and 0.5 mmol octadecyl phosphonic acid (97%, Alfa Aesar) and degassed triethylamine (10 mL) were added into a 25 mL round-bottom flask. The solution was heated with stirring to 120 °C for 30 min under the vacuum condition to remove impurities with a low boiling point and oxygen. The solution was heated to 180 °C under an N₂ atmosphere for 30 min and subsequently heated to 270 °C for another 30 min. After the reaction, the heating mantle was removed, and the solution was naturally cooled to room temperature. The solution was extracted into a centrifuge tube and the antisolvent containing acetone and methanol was added to wash and separate from the reaction solvent via centrifugation and subsequent removal of the supernatant solution. The above washing and centrifugation processes were repeated three times. Finally, the CuO_x NPs were dispersed in hexane and stored in an N₂-purged glovebox.

Electrode Preparation. Electrodes were prepared by drop-casting CuO_x NPs solution dispersed in hexane on a graphite foil (100 μm) with a geometric area of 1 cm² (mass loading ~0.25 mg/cm²). The concentration of the CuO_x NP solution was quantified by using inductively coupled plasma mass spectrometry (Agilent 7900). For the carbon black-supported CuO_x NPs (CuO_x NPs/CB), carbon black (Sigma-Aldrich) was sonicated in a mixture of isopropyl alcohol and Nafion 117 (Sigma-Aldrich) solution (65:1 in volume) for 10 min. The CuO_x NPs in hexane were mixed with the resulting solution (C/Cu mass ratio 1.6) with a further 30 min sonication. The resulting catalyst ink (400 μL) was drop-cast onto a 4 cm² graphite foil, resulting in a final mass loading of ~0.125 mg/cm² for the CuO_x NPs/CB electrode.

Characterization. The FEI ThemIS 60-300 (Thermo Fisher Scientific) transmission electron microscope with an X-FEG gun was exploited to acquire transmission electron microscopy (TEM), scanning TEM (STEM), and STEM-energy dispersive X-ray spectroscopy (EDS) data. The microscope was operated at an accelerating voltage of 300 kV and is equipped with an image aberration corrector (with a TEM spatial resolution limit of 70 pm) and the Bruker SuperX EDS detector (with a solid angle of 0.7 steradians). The Ceta2 CMOS camera and a high-angle annular dark field detector were used for TEM and STEM imaging, respectively. The Quanta 250 FEG (FEI Company) scanning electron microscope (SEM) with the Bruker QUANTAX 200 energy dispersive X-ray spectrometer was used to record SEM and energy dispersive spectroscopy (EDS) data. The operating voltage of 10 kV was set to obtain SEM and SEM-EDS results. For the ex situ characterization of CuO_x NPs and CuO_x NPs/CB electrode, the electrode was extracted by disassembling the in situ cell and stored in an argon-filled glovebox without undergoing any washing steps until subsequent TEM and SEM characterizations. The ex situ SEM measurements of the electrode were performed without any post-treatment. For ex situ TEM measurements, ultrathin carbon films coated on Cu TEM grids were subjected to a 5 s treatment with O₂ plasma, followed by the application of 25 μL of isopropyl alcohol onto the grids. The treated grids were gently rubbed with the ex situ electrode sample to transfer Cu nanostructures onto the TEM grids.

In Situ Small-Angle X-ray Scattering (SAXS). In situ SAXS measurements were performed at Stanford Synchrotron Radiation Lightsource (SSRL) beamline 1–5. The in situ experiments were carried out under CO₂ and Ar conditions using a modified cell design based on our previous study.¹² A hybrid catalyst-bonded membrane reactor that had been developed previously was modified to accommodate Si₃N₄ windows (100 nm thickness, CX9060C, Norcada) on both the cathode and anode sides. The Si₃N₄ windows were compression sealed to the cell body by 3D-printed plastic lids with silicon elastomer used as a gasket. A Pt mesh with an opening in the center for the X-ray beam was used as a counter electrode (C.E.), and 0.5 M KHCO₃ electrolytes circulated in both cathode and anode chambers, separated by an anion-exchange membrane. The CO₂ gas was introduced at a flow rate of 10 sccm in reservoirs of catholyte and anolyte that were circulated into both cathode and anode chambers, respectively. The leakless Ag/AgCl reference electrode (R.E.) was placed adjacent to the CuO_x NPs (working electrode) electrode. The

reactor volume was minimized to decrease the thickness of the electrolyte in the X-ray beam path (~6 mm), resulting in ~21% transmission at an X-ray energy of 13 keV. In both chambers, 0.5 M KHCO₃ aqueous electrolyte saturated with CO₂ gas (99.999%) flowed using a peristaltic pump at 2.5 mL/min, entering from the bottom and exiting from the top of the cell. For the Ar conditions, 0.5 M K₄H_{3-x}PO₄ electrolytes saturated with Ar gas (99.999%) flowed through both chambers at the same flow rate. To detach excess bubbles in the X-ray beam path, 5 mM sodium *p*-toluenesulfonate (Sigma-Aldrich) was added to the electrolytes. The prepared electrolytes were pre-cleaned with a chelating agent (Chelex 100, Sigma-Aldrich) to remove any metal impurities. The wavelength λ of the X-ray was 0.953725 Å (13 keV) with a beam spot size of 500 × 500 μm². The exposure time for each frame was set to be 1 min. The SAXS patterns were collected using a Rayonix 165 SX CCD area detector with 79 μm pixel sizes and 165 mm² diameter active area. The Pilatus 1 M fast detector was used for the carbon black-supported samples. The sample-to-detector distance for SAXS was calibrated to be 2879.8 mm using a silver behenate standard, resulting in a minimum scattering vector Q of ~0.006 Å⁻¹. 2D SAXS data were integrated into 1D scattering curves I(q) presented as a function of scattering vector q = (4π/λ)sin(θ/2), where λ is the wavelength of the incident X-ray and θ is the scattering angle. The absolute intensity calibration was performed using a glassy carbon standard. The SAXS data are on an arbitrary scale because the thickness of the CuO_x NPs electrode was not used to normalize the data.

In Situ X-ray Absorption Spectroscopy. In situ X-ray absorption spectroscopy (XAS) measurements were conducted at the Stanford Synchrotron Radiation Lightsource (SSRL) on beamline 2–2 at the Cu K-edge (8979 eV). The in situ experiments were performed under CO₂ and Ar gas conditions using a cylindrical cell described in Figure S14. The cell was placed in a vertical geometry with the 0.5 M KHCO₃ electrolyte being pumped through the cell using a peristaltic pump at 2.5 mL/min as it was continuously sparged with high-purity CO₂ (99.998%, Airgas) flowing at 10 sccm. A leakless Ag/AgCl reference electrode (ET072-1, eDAQ) was used to measure the applied potentials, but the reference electrode was calibrated versus a standard hydrogen electrode (SHE) and potential values are reported for the KCl saturated Ag/AgCl electrode. The cylindrical cell was mounted at a 45° angle to the incident X-ray beam, and the fluorescence signal exiting the cell was collected at 90° relative to the incident beam. The incident beam energy was tuned using a water-cooled Si(220) monochromator and the ion chamber was filled with N₂ gas. Energy calibration was conducted using a Cu reference foil, defining 8979 eV as the maximum of the first inflection point of the first derivative of the reference spectrum. For the in situ measurements, the continuous-scan mode was used by recording the spectra from 8850 to 9200 eV to cover the Cu K-edge, and each scan took ~15 s. A Cu foil was scanned simultaneously for every scan taken to check for any energy shift. The XANES scans were repeated until no more spectral changes were observed.

Data Analysis. In situ SAXS data were analyzed using the unified fit model implemented in the Irena package (version 2.71, IgorPro, Wave Metrics Inc.) after background subtraction. The scattering signal from the graphite foil immersed in the electrolytes with the relevant applied potentials was measured and used as the background. For the carbon black supported samples, the scattering signal from the carbon black deposited on the graphite foil with flowing electrolyte and applied potentials were collected as the background. The unified fit model can evaluate the collected scattering data by separating it into different structural levels. We considered all the CuO_x NPs samples having two structural levels where the small primary NPs form as the first level and the resulting aggregates as the second level. More details about the theory and fitting process of the unified fit model are described in the Supporting Information. In situ XANES data analysis was conducted using the Athena software package. Pre-edge and post-edge backgrounds were subtracted from the XAS spectra, and the resulting spectra were normalized by edge height. To account for potential variations in the thickness of graphite foil

substrates and deposited CuO_x NP layer, we employed normalization of the edge step by the initial values at open circuit conditions.

Electrochemical Measurements. For all chronoamperometry (CA) measurements, linear sweep voltammetry (LSV) to an applied potential of -1.1 V vs RHE at 100 mV⁻¹ was done before the CA, as this was found to improve the stability of the current profile. At the beginning of the CA, the solution resistance is recorded; during the in situ SAXS and in situ XAS measurements, the potentials were applied for at least 1 h without on-the-fly solution resistance compensation. Instead, the potentials were manually corrected after the measurements using a predetermined resistance. This resistance was determined by fitting the high-frequency region of the electrochemical impedance spectroscopy data. For the product measurement experiments, a two-compartment compression cell previously described in the literature was used,⁴⁷ with a slight modification by using a gas dispersion frit to introduce the CO₂ gas into the cathode compartment; a CO₂ flow rate of 20 mL/min was introduced into both cathode and anode compartments continuously throughout the experiment. The potentials were corrected for 85% of the solution resistance using the built-in *iR* compensation method with current interruption mode. For each set of experimental data points at one given set of reaction conditions, one sample was used; the electrolyte was replaced for each measurement after rinsing the cell with DI water, and the electrolyte was presaturated with CO₂ for at least 1 h before each measurement. Each sample was prepared identically to those used for the in situ experiments, and all electrolytes used were the same purity and had the same supplier as for the in situ experiments, and the electrolyte was purified with Chelex before use. For gas product analysis, the gas outlet of the two-compartment compression cell was connected to an MG3 gas chromatograph (SRI). During electrolysis, gas products were injected online as 1 mL aliquots into the GC at evenly spaced intervals; at least three samples of gas products were collected and averaged for the set of reaction conditions; standard references were used for calibration to determine the gas product concentration and then calculate the faradaic efficiency of electrolysis. The liquid phase products were quantified with 1D ¹H NMR (600 MHz, Varian Inova) by sampling 700 μL aliquots of the electrolyte after electrolysis; standard curves using internal standards were used to quantify the liquid product concentration and calculate the faradaic efficiency for these products.

■ ASSOCIATED CONTENT

Data Availability Statement

Additional data that support the findings of this study are reported in the [Supporting Information](#). Any additional data are available from the corresponding author upon request. In situ SAXS data were analyzed using the unified fit model implemented in the Irena package (version 2.71, IgorPro, Wave Metrics Inc.). The code for Irena package can be found at <https://usaxs.xray.aps.anl.gov/software/irena> with Ilavsky, J.; Jemian, P. R. Irena: tool suite for modeling and analysis of small-angle scattering. *J. Appl. Crystallogr.* **2009**, *42*, 347–353. The version of the code employed for this study is version 2.71. In situ XANES data analysis was conducted using the Athena software package. The code for Athena can be found at <https://bruceravel.github.io/demeter/documents/Athena/index.html> with Ravel, B.; Newville, M. ATHENA, ARTEMIS, HEPHAESTUS: data analysis for X-ray absorption spectroscopy using IFEFFIT. *J. Synchrotron Radiat.* **2005**, *12*, 537–541.

SI Supporting Information

The Supporting Information is available free of charge at <https://pubs.acs.org/doi/10.1021/jacs.4c14720>.

Detailed theoretical background of the unified fit model, along with additional microscopic and spectroscopic data, including SEM, TEM, EDX, XRD, in situ SAXS, and in situ XANES analyses ([PDF](#))

■ AUTHOR INFORMATION

Corresponding Authors

Soo Hong Lee – Liquid Sunlight Alliance, Lawrence Berkeley National Laboratory, Berkeley, California 94720, United States; Chemical Sciences Division, Lawrence Berkeley National Laboratory, Berkeley, California 94720, United States; Chemical & Process Technology Division, Korea Research Institute of Chemical Technology (KRICT), Daejeon 34114, South Korea; orcid.org/0000-0002-2734-9654; Email: shlee2@kRICT.re.kr

Thomas F. Jaramillo – SUNCAT Center for Interface Science and Catalysis, SLAC National Accelerator Laboratory, Menlo Park, California 94025, United States; Department of Chemical Engineering, Stanford University, Stanford, California 94305, United States; orcid.org/0000-0001-9900-0622; Email: jaramillo@stanford.edu

Walter S. Drisdell – Liquid Sunlight Alliance, Lawrence Berkeley National Laboratory, Berkeley, California 94720, United States; Chemical Sciences Division, Lawrence Berkeley National Laboratory, Berkeley, California 94720, United States; orcid.org/0000-0002-8693-4562; Email: wdsdrisdell@lbl.gov

Authors

Jaime E. Avilés Acosta – Department of Materials Science and Engineering, Stanford University, Stanford, California 94305, United States; SUNCAT Center for Interface Science and Catalysis, SLAC National Accelerator Laboratory, Menlo Park, California 94025, United States

Daewon Lee – Materials Sciences Division, Lawrence Berkeley National Laboratory, Berkeley, California 94720, United States; Department of Materials Science and Engineering, University of California, Berkeley, California 94720, United States

David M. Larson – Liquid Sunlight Alliance, Lawrence Berkeley National Laboratory, Berkeley, California 94720, United States; Chemical Sciences Division, Lawrence Berkeley National Laboratory, Berkeley, California 94720, United States; Present Address: Twelve Benefit Corporation, 614 Bancroft Way, Berkeley, California 94710, United States

Hui Li – Liquid Sunlight Alliance, Lawrence Berkeley National Laboratory, Berkeley, California 94720, United States; Chemical Sciences Division, Lawrence Berkeley National Laboratory, Berkeley, California 94720, United States

Junjie Chen – SUNCAT Center for Interface Science and Catalysis, SLAC National Accelerator Laboratory, Menlo Park, California 94025, United States; Department of Chemical Engineering, Stanford University, Stanford, California 94305, United States; orcid.org/0000-0002-0954-1028

Jinyoung Lee – Department of Chemical Engineering, Stanford University, Stanford, California 94305, United States; School of Energy and Chemical Engineering, Ulsan National Institute of Science and Technology (UNIST), Ulsan 44919, Republic of Korea

Ezgi Erdem – SUNCAT Center for Interface Science and Catalysis, SLAC National Accelerator Laboratory, Menlo Park, California 94025, United States; Department of Chemical Engineering, Stanford University, Stanford, California 94305, United States

Dong Un Lee – Department of Chemical Engineering, Stanford University, Stanford, California 94305, United States; orcid.org/0000-0001-7591-5350

Sarah J. Blair – SUNCAT Center for Interface Science and Catalysis, SLAC National Accelerator Laboratory, Menlo Park, California 94025, United States; Department of Chemical Engineering, Stanford University, Stanford, California 94305, United States; Present Address: Chemistry and Nanoscience Department, National Renewable Energy Laboratory, Golden, Colorado 80401, United States.; orcid.org/0000-0001-6680-0199

Alessandro Gallo – SUNCAT Center for Interface Science and Catalysis, SLAC National Accelerator Laboratory, Menlo Park, California 94025, United States; Present Address: Sila Nanotechnologies, 2470 Mariner Square Loop, Alameda, California 94051, United States.; orcid.org/0000-0003-4687-8188

Haimei Zheng – Materials Sciences Division, Lawrence Berkeley National Laboratory, Berkeley, California 94720, United States; Department of Materials Science and Engineering, University of California, Berkeley, California 94720, United States.; orcid.org/0000-0003-3813-4170

Adam C. Nielander – SUNCAT Center for Interface Science and Catalysis, SLAC National Accelerator Laboratory, Menlo Park, California 94025, United States

Christopher J. Tassone – Stanford Synchrotron Radiation Lightsource, SLAC National Accelerator Laboratory, Menlo Park, California 94025, United States

Complete contact information is available at:

<https://pubs.acs.org/10.1021/jacs.4c14720>

Author Contributions

^{|||}S.H.L. and J.E.A.A. contributed equally to this work.

Notes

The authors declare no competing financial interest.

ACKNOWLEDGMENTS

Electrochemical flow cell assembly, in situ SAXS, and XANES measurements of CuO_x NPs were conducted based on work performed by the Liquid Sunlight Alliance, which is supported by the U.S. Department of Energy, Office of Science, Office of Basic Energy Sciences, Fuels from Sunlight Hub under award number DE-SC0021266. The material for the synthesis of CuO_x NPs, as well as the design and fabrication of in situ SAXS and XANES cell, were supported by the Joint Center for Artificial Photosynthesis, a DOE Energy Innovation Hub, supported through the Office of Science of the U.S. Department of Energy, under award no. DE-SC0004993. Use of the Stanford Synchrotron Radiation Lightsource, SLAC National Accelerator Laboratory, is supported by the U.S. Department of Energy, Office of Science, Office of Basic Energy Sciences under contract no. DE-AC02-76SF00515. The SAXS data analysis is supported by the KRICT project (no. KK2411-00) from the Korea Research Institute of Chemical Technology (KRICT). The electrode fabrication, electrochemical testing, product quantification and analysis performed are supported by a cooperative research and development sponsored by TotalEnergies American Services, Inc. (affiliate of TotalEnergies SE) under the agreement number TC02307. Brain link project (2022H1D3A3A01081140) funded by National Research Foundation of Korea (NRF) provided funding for Jinyoung Lee. The SEM, EDS, TEM, and STEM characterizations at the Molecular Foundry, Lawrence Berkeley National Laboratory,

and their analysis are supported by the U.S. Department of Energy, Office of Science, Office of Basic Energy Sciences (BES), Materials Sciences and Engineering Division under contract no. DE-AC02-05-CH11231 within the in situ TEM program (KC22ZH) and the Office of Science, Office of Basic Energy Sciences, of the U.S. Department of Energy under contract no. DE-AC02-05CH11231. Part of this work was performed at the Stanford Nano Shared Facilities (SNSF), supported by the National Science Foundation under award ECCS-2026822. E.E. acknowledges the Stanford Prism Baker Fellowship. We thank Dr. Soon Gu Kwon who makes Matlab codes for SAXS data normalization and discussion for SAXS fittings. D.L. acknowledges the Kwanjeong Study Abroad Scholarship from the KEF (Kwanjeong Educational Foundation) (KEF-2019).

REFERENCES

- (1) Wakerley, D.; Lamaison, S.; Wicks, J.; Clemens, A.; Feaster, J.; Corral, D.; Jaffer, S. A.; Sarkar, A.; Fontecave, M.; Duoss, E. B.; et al. Gas diffusion electrodes, reactor designs and key metrics of low-temperature CO₂ electrolyzers. *Nat. Energy* **2022**, *7*, 130–143.
- (2) Jordaan, S. M.; Wang, C. Electrocatalytic conversion of carbon dioxide for the Paris goals. *Nat. Catal.* **2021**, *4*, 915–920.
- (3) Birdja, Y. Y.; Pérez-Gallent, E.; Figueiredo, M. C.; Göttle, A. J.; Calle-Vallejo, F.; Koper, M. T. M. Advances and challenges in understanding the electrocatalytic conversion of carbon dioxide to fuels. *Nat. Energy* **2019**, *4*, 732–745.
- (4) Liu, Z.; Yang, H.; Kutz, R.; Masel, R. I. CO₂ Electrolysis to CO and O₂ at High Selectivity, Stability and Efficiency Using Sustainion Membranes. *J. Electrochem. Soc.* **2018**, *165*, J3371.
- (5) Xu, Y.; Edwards, J. P.; Liu, S.; Miao, R. K.; Huang, J. E.; Gabardo, C. M.; O'Brien, C. P.; Li, J.; Sargent, E. H.; Sinton, D. Self-Cleaning CO₂ Reduction Systems: Unsteady Electrochemical Forcing Enables Stability. *ACS Energy Lett.* **2021**, *6*, 809–815.
- (6) Stephens, I. E. L.; Chan, K.; Bagger, A.; Boettcher, S. W.; Bonin, J.; Boutin, E.; Buckley, A. K.; Buonsanti, R.; Cave, E. R.; Chang, X.; et al. 2022 roadmap on low temperature electrochemical CO₂ reduction. *J. Phys. Energy* **2022**, *4*, 042003.
- (7) Li, F.; Medvedeva, X. V.; Medvedev, J. J.; Khairullina, E.; Engelhardt, H.; Chandrasekar, S.; Guo, Y.; Jin, J.; Lee, A.; Thérien-Aubin, H.; et al. Interplay of electrochemical and electrical effects induces structural transformations in electrocatalysts. *Nat. Catal.* **2021**, *4*, 479–487.
- (8) Mom, R. V.; Sandoval-Diaz, L.-E.; Gao, D.; Chuang, C.-H.; Carbonio, E. A.; Jones, T. E.; Arrigo, R.; Ivanov, D.; Hävecker, M.; Roldan Cuenya, B.; et al. Assessment of the Degradation Mechanisms of Cu Electrodes during the CO₂ Reduction Reaction. *ACS Appl. Mater. Interfaces* **2023**, *15*, 30052–30059.
- (9) Popović, S.; Smiljanić, M.; Jovanović, P.; Vavra, J.; Buonsanti, R.; Hodnik, N. Stability and Degradation Mechanisms of Copper-Based Catalysts for Electrochemical CO₂ Reduction. *Angew. Chem., Int. Ed.* **2020**, *59*, 14736–14746.
- (10) Lee, S. H.; Lin, J. C.; Farmand, M.; Landers, A. T.; Feaster, J. T.; Avilés Acosta, J. E.; Beeman, J. W.; Ye, Y.; Yano, J.; Mehta, A.; et al. Oxidation State and Surface Reconstruction of Cu under CO₂ Reduction Conditions from In Situ X-ray Characterization. *J. Am. Chem. Soc.* **2021**, *143* (2), 588–592.
- (11) Cheng, W.; Chen, Z.; Wu, X.; Wu, Z.; Wang, X.; Zhao, M.; Liu, H.; Jia, H.; Wang, C.; Wang, X.; et al. Anomalous Small-Angle X-ray Scattering and Its Application in the Dynamic Reconstruction of Electrochemical CO₂ Reduction Catalysts. *Symmetry* **2023**, *15*, 1034.
- (12) Lee, S. H.; Sullivan, I.; Larson, D. M.; Liu, G.; Toma, F. M.; Xiang, C.; Drisdell, W. S. Correlating Oxidation State and Surface Area to Activity from Operando Studies of Copper CO Electroreduction Catalysts in a Gas-Fed Device. *ACS Catal.* **2020**, *10*, 8000–8011.

- (13) Wang, X.; Jiang, Y.; Mao, K.; Gong, W.; Duan, D.; Ma, J.; Zhong, Y.; Li, J.; Liu, H.; Long, R.; et al. Identifying an Interfacial Stabilizer for Regeneration-Free 300 h Electrochemical CO₂ Reduction to C₂ Products. *J. Am. Chem. Soc.* **2022**, *144*, 22759–22766.
- (14) Manthiram, K.; Surendranath, Y.; Alivisatos, A. P. Dendritic Assembly of Gold Nanoparticles during Fuel-Forming Electrocatalysis. *J. Am. Chem. Soc.* **2014**, *136*, 7237–7240.
- (15) Redmond, P. L.; Hallock, A. J.; Brus, L. E. Electrochemical Ostwald Ripening of Colloidal Ag Particles on Conductive Substrates. *Nano Lett.* **2005**, *5*, 131–135.
- (16) Vavra, J.; Shen, T.-H.; Stoian, D.; Tileli, V.; Buonsanti, R. Real-time Monitoring Reveals Dissolution/Redeposition Mechanism in Copper Nanocatalysts during the Initial Stages of the CO₂ Reduction Reaction. *Angew. Chem., Int. Ed.* **2021**, *60*, 1347–1354.
- (17) Arán-Ais, R. M.; Rizo, R.; Grosse, P.; Algara-Siller, G.; Dembélé, K.; Plodinec, M.; Lunkenbein, T.; Chee, S. W.; Cuenya, B. R. Imaging electrochemically synthesized Cu₂O cubes and their morphological evolution under conditions relevant to CO₂ electroreduction. *Nat. Commun.* **2020**, *11*, 3489.
- (18) Vavra, J.; Ramona, G. P. L.; Dattila, F.; Kormányos, A.; Priamushko, T.; Albertini, P. P.; Loiudice, A.; Cherevko, S.; Lopéz, N.; Buonsanti, R. Solution-based Cu⁺ transient species mediate the reconstruction of copper electrocatalysts for CO₂ reduction. *Nat. Catal.* **2024**, *7*, 89–97.
- (19) Speck, F. D.; Cherevko, S. Electrochemical copper dissolution: A benchmark for stable CO₂ reduction on copper electrocatalysts. *Electrochem. Commun.* **2020**, *115*, 106739.
- (20) Mu, S.; Lu, H.; Wu, Q.; Li, L.; Zhao, R.; Long, C.; Cui, C. Hydroxyl radicals dominate reoxidation of oxide-derived Cu in electrochemical CO₂ reduction. *Nat. Commun.* **2022**, *13*, 3694.
- (21) Yang, Y.; Shao, Y.-T.; Lu, X.; Yang, Y.; Ko, H.-Y.; DiStasio, R. A., Jr.; DiSalvo, F. J.; Muller, D. A.; Abruña, H. D. Elucidating Cathodic Corrosion Mechanisms with Operando Electrochemical Transmission Electron Microscopy. *J. Am. Chem. Soc.* **2022**, *144*, 15698–15708.
- (22) Kolle-Görge, E.; Fortunato, G.; Ledendecker, M. Catalyst Stability in Aqueous Electrochemistry. *Chem. Mater.* **2022**, *34*, 10223–10236.
- (23) Osowiecki, W. T.; Nussbaum, J. J.; Kamat, G. A.; Katsoukis, G.; Ledendecker, M.; Frei, H.; Bell, A. T.; Alivisatos, A. P. Factors and Dynamics of Cu Nanocrystal Reconstruction under CO₂ Reduction. *ACS Appl. Energy Mater.* **2019**, *2*, 7744–7749.
- (24) Li, Y.; Kim, D.; Louisa, S.; Xie, C.; Kong, Q.; Yu, S.; Lin, T.; Aloni, S.; Fakra, S. C.; Yang, P. Electrochemically scrambled nanocrystals are catalytically active for CO₂-to-multicarbon. *Proc. Natl. Acad. Sci. U.S.A.* **2020**, *117*, 9194–9201.
- (25) Yang, Y.; Louisa, S.; Yu, S.; Jin, J.; Roh, I.; Chen, C.; Fonseca Guzman, M. V.; Feijóo, J.; Chen, P.-C.; Wang, H.; et al. Operando studies reveal active Cu nanograins for CO₂ electroreduction. *Nature* **2023**, *614*, 262–269.
- (26) Larrazábal, G. O.; Strøm-Hansen, P.; Heli, J. P.; Zeiter, K.; Therkildsen, K. T.; Chorkendorff, I.; Seger, B. Analysis of Mass Flows and Membrane Cross-over in CO₂ Reduction at High Current Densities in an MEA-Type Electrolyzer. *ACS Appl. Mater. Interfaces* **2019**, *11*, 41281–41288.
- (27) Corral, D.; Lee, D. U.; Ehlinger, V. M.; Nitopi, S.; Avilés Acosta, J. E.; Wang, L.; King, A. J.; Feaster, J. T.; Lin, Y.-R.; Weber, A. Z.; et al. Bridging knowledge gaps in liquid- and vapor-fed CO₂ electrolysis through active electrode area. *Chem Catal.* **2022**, *2*, 3239–3253.
- (28) Kováts, P.; Thévenin, D.; Zähringer, K. Influence of viscosity and surface tension on bubble dynamics and mass transfer in a model bubble column. *Int. J. Multiphase Flow* **2020**, *123*, 103174.
- (29) Beaucage, G.; Kammler, H. K.; Pratsinis, S. E. Particle size distributions from small-angle scattering using global scattering functions. *J. Appl. Crystallogr.* **2004**, *37*, 523–535.
- (30) Xu, F.; Zhang, H.; Ilavsky, J.; Stanciu, L.; Ho, D.; Justice, M. J.; Petrace, H. I.; Xie, J. Investigation of a Catalyst Ink Dispersion Using Both Ultra-Small-Angle X-ray Scattering and Cryogenic TEM. *Langmuir* **2010**, *26*, 19199–19208.
- (31) Yang, F.; Xin, L.; Uzunoglu, A.; Qiu, Y.; Stanciu, L.; Ilavsky, J.; Li, W.; Xie, J. Investigation of the Interaction between Nafion Ionomer and Surface Functionalized Carbon Black Using Both Ultrasmall Angle X-ray Scattering and Cryo-TEM. *ACS Appl. Mater. Interfaces* **2017**, *9*, 6530–6538.
- (32) Kehres, J.; Jakobsen, J. G.; Andreassen, J. W.; Wagner, J. B.; Liu, H.; Molenbroek, A.; Sehested, J.; Chorkendorff, I.; Vegge, T. Dynamical properties of a Ru/MgAl₂O₄ catalyst during reduction and dry methane reforming. *J. Phys. Chem. C* **2012**, *116*, 21407–21415.
- (33) Sztucki, M.; Narayanan, T.; Beaucage, G. In situ study of aggregation of soot particles in an acetylene flame by small-angle x-ray scattering. *J. Appl. Phys.* **2007**, *101*, 114304.
- (34) Beaucage, G. Small-Angle Scattering from Polymeric Mass Fractals of Arbitrary Mass-Fractal Dimension. *J. Appl. Crystallogr.* **1996**, *29*, 134–146.
- (35) Ho, P. S.; Kwok, T. Electromigration in metals. *Rep. Prog. Phys.* **1989**, *52*, 301.
- (36) Simonsen, S. B.; Chorkendorff, I.; Dahl, S.; Skoglundh, M.; Sehested, J.; Helveg, S. Direct Observations of Oxygen-induced Platinum Nanoparticle Ripening Studied by In Situ TEM. *J. Am. Chem. Soc.* **2010**, *132*, 7968–7975.
- (37) Pankhurst, J. R.; Iyengar, P.; Loiudice, A.; Mensi, M.; Buonsanti, R. Metal–ligand bond strength determines the fate of organic ligands on the catalyst surface during the electrochemical CO₂ reduction reaction. *Chem. Sci.* **2020**, *11*, 9296–9302.
- (38) Huang, J.; Hörmann, N.; Oveisi, E.; Loiudice, A.; De Gregorio, G. L.; Andreussi, O.; Marzari, N.; Buonsanti, R. Potential-induced nanoclustering of metallic catalysts during electrochemical CO₂ reduction. *Nat. Commun.* **2018**, *9*, 3117.
- (39) Grosse, P.; Yoon, A.; Rettenmaier, C.; Herzog, A.; Chee, S. W.; Roldan Cuenya, B. Dynamic transformation of cubic copper catalysts during CO₂ electroreduction and its impact on catalytic selectivity. *Nat. Commun.* **2021**, *12*, 6736.
- (40) Krumbein, S. J. Electrolytic models for metallic electro-migration failure mechanisms. *IEEE Trans. Reliab.* **1995**, *44*, 539–549.
- (41) Maekawa, K.; Mori, K.; Suzumura, N.; Honda, K.; Hirose, Y.; Asai, K.; Uedono, A.; Kojima, M. Impact of Al in Cu alloy interconnects on electro and stress migration reliabilities. *Microelectron. Eng.* **2008**, *85*, 2137–2141.
- (42) Mariano, R. G.; McKelvey, K.; White, H. S.; Kanan, M. W. Selective increase in CO₂ electroreduction activity at grain-boundary surface terminations. *Science* **2017**, *358*, 1187–1192.
- (43) Oates, A. S. Strategies to Ensure Electromigration Reliability of Cu/Low-k Interconnects at 10 nm. *ECS J. Solid State Sci. Technol.* **2015**, *4*, N3168.
- (44) Zhong, M.; Tran, K.; Min, Y.; Wang, C.; Wang, Z.; Dinh, C.-T.; De Luna, P.; Yu, Z.; Rasouli, A. S.; Brodersen, P.; et al. Accelerated discovery of CO₂ electrocatalysts using active machine learning. *Nature* **2020**, *581*, 178–183.
- (45) Yoo, J. M.; Shin, H.; Chung, D. Y.; Sung, Y.-E. Carbon Shell on Active Nanocatalyst for Stable Electrocatalysis. *Acc. Chem. Res.* **2022**, *55*, 1278–1289.
- (46) Okatenko, V.; Loiudice, A.; Newton, M. A.; Stoian, D. C.; Blokhina, A.; Chen, A. N.; Rossi, K.; Buonsanti, R. Alloying as a Strategy to Boost the Stability of Copper Nanocatalysts during the Electrochemical CO₂ Reduction Reaction. *J. Am. Chem. Soc.* **2023**, *145*, 5370–5383.
- (47) Kuhl, K. P.; Cave, E. R.; Abram, D. N.; Jaramillo, T. F. New insights into the electrochemical reduction of carbon dioxide on metallic copper surfaces. *Energy Environ. Sci.* **2012**, *5*, 7050–7059.